Friction https://mc03.manuscriptcentral.com/friction
https://doi.org/10.26599/FRICT.2026.9441230

Research Article

Intelligent self-evolving design method of high-load-bearing hydrostatic oil groove

Xiaolong Zhang[1], Kaiming Zheng[1], Kou Du[2], Hongbin Lin[1], Shaobo Sun[3], Junhui Zhang[1], Bing Xu[1], Huayong Yang[1], Chao Zhang[*1]

[1] *State Key Laboratory of Fluid Power Components & Mechatronic Systems, Zhejiang University, Hangzhou 310058, China*

[2] *Inner Mongolia North Heavy Industries Group Corp., Ltd., Baotou 014033, China*

[3] *Zenmax Hydraulic Technology Co., Ltd. Qinhuangdao 066006, China*

* Corresponding author: Chao Zhang, E-mail: chao.zhang@zju.edu.cn

Received: September 24, 2025; Revised: January 11, 2026; Accepted: February 4, 2026

Abstract: Hydrostatic oil grooves in the friction pair are responsible for guiding, storing, and distributing lubricating oil, widely applied to ultra-high-power hydraulic motors of tunnel boring machines, aerospace variable pumps, and hydrostatic precision guideways/spindles of high-end industrial mother machines, etc. The traditional design methods for oil groove patterns highly rely on the designer's experience and size optimization of preset shapes, making it difficult to achieve optimal lubrication. For that, this study proposes the intelligent self-evolving design method of oil grooves, in which the AI-assisted generalized pattern search algorithm (GPS+AI) is designed to make an oil groove pattern self-evolve towards maximizing load-bearing capacity according to the friction pair's contact force feedback from a lubrication model. The designed oil groove pattern is machined onto the piston of a hydraulic motor and is experimentally evaluated for its lubrication load-bearing capacity through the home-made quasi-actual roller-piston pair testing rig. Comparing two traditional oil grooves, the new oil groove can reduce the friction torque (contact force) by a maximum of 88%, which is very significant for improving efficiency and lifespan of ultra-high power hydraulic motors (power > 10^6 W), especially under the dual-carbon target.

Keywords: Design, Oil groove, AI, Lubrication, Hydraulic motor

Nomenclature

$\boldsymbol{P}_{\mathrm{s}}$	The point set on a friction pair
$\boldsymbol{P}_{\mathrm{f}}$	The set of anchor points from the rectangular design region
f_{m}	A mapping function
P_{si}	si^{th} anchor point
φ_{si}	The value of si^{th} anchor point value
g_{ai}	The height value of the ai^{th} point on the controlled surface
N	The total number of anchor points
Θ	The Gaussian covariance function
w_{si}	The influence weight of the anchor point P_{si}
l_0, l_1, l_2	The three linear correction factors
l_{s}	The shape parameter
$\mathrm{C_r}$	A constant

l_{m}	The minimum distance between the anchor points
L_{d}	The longest side length of the rectangular design domain
$\Theta_{a,b}$	The Θ value of the a^{th} anchor point and the b^{th} anchor point
$x_{si=N}$, $y_{si=N}$	The coordinates of the N^{th} anchor point
w_N	The weights of the N^{th} anchor point
φ_N	The values of the N^{th} anchor point
G	Functional representation of the oil groove pattern
$\boldsymbol{\varphi}$	A column vector consisting of the anchor point values φ_{si}
F_{c}	The contact force
Ω	The oil film region
Ω_{e}	The effective region
$\boldsymbol{\varphi}^{j-1}$, $\boldsymbol{\varphi}^{j}$	The current base point and the new base point
$\boldsymbol{s}_i^j$	The trial point
M_{G}	The number of oil groove patterns when the AI is first started
G_*^j	The current optimal oil groove pattern
M_{g}	The minimum number of oil groove patterns provided to the GPS by AI in each iteration
M_{n}	The minimum number of increased oil groove patterns when the AI is again trained
Δm^j	The GPS algorithm step size
$\boldsymbol{V}$	The pattern vectors
$\boldsymbol{v}_i$	An N-dimensional column vector
$\boldsymbol{s}_*^j$	The improved trial point
κ_{e}, κ_{c}	The expansion and contraction factors of the step size

$\boldsymbol{G}_{\mathrm{p}}$	The matrix of the pixelated oil groove pattern
$\boldsymbol{\delta}^{i}$	A group of disturbances
$\boldsymbol{\delta}_{k}^{i}$	A disturbance
N_r	Number of disturbances in the $\boldsymbol{\delta}^{i}$
L_{H}, L_{W}	The increased height and width of the image after padding
H_{G},W_{G},D_{G}	The height, width, and depth (number of channels) of the input image
H_{s}, W_{s}	The step size of the convolution kernel moving along the direction of height and width
H_{k}. W_{k}	The height and width of the convolution kernel
$\boldsymbol{I}_{\mathrm{c}}$	The input of the convolution operation
k_{c}	The $k_{\mathrm{c}}^{\mathrm{th}}$ convolution kernel of the current layer
$\boldsymbol{X}_{\mathrm{c}}^{kc}\left(i,j\right)$	The element of the i^{th} row and j^{th} column in the feature map ($\boldsymbol{X}_{\mathrm{c}}$) from the $k_{\mathrm{c}}^{\mathrm{th}}$ convolution kernel
*	The convolution operator
H_{I}, W_{I}, D_{I}	The height, width, and depth of the input image ($\boldsymbol{I}_{\mathrm{c}}$)
$\boldsymbol{K}_{\mathrm{c}}$	The convolution kernel (weight matrix)
b^{kc}	The bias of the $k_{\mathrm{c}}^{\mathrm{th}}$ convolution kernel
σ_{L}	The parameter of the activation function
$\boldsymbol{Y}_{\mathrm{c1}}$	The output of the C1 layer
$\boldsymbol{Y}_{\mathrm{c3}}$	The output from the C3 layer
H_{p}, W_{p}	The height and width of the pooling kernel
$\boldsymbol{X}_{\mathrm{F}}$	The output of the flattening layer
$\boldsymbol{K}_{\mathrm{f1}}$,$\boldsymbol{K}_{\mathrm{f2}}$,$\boldsymbol{K}_{\mathrm{f3}}$	The weights of the three-layer fully connected layers

$\boldsymbol{b}_{f1},\boldsymbol{b}_{f2},\boldsymbol{b}_{f3}$	The biases of the three-layer fully connected layers
F_{cpk}	The minimum contact force found by the k^{th} individual up to now
$\boldsymbol{\delta}_{pbestk}$	The optimal solution currently searched by individuals
F_{cnk}	The minimum contact force in the subgroup
$\boldsymbol{\delta}_{nbestk}$	The optimal solution currently searched in the k^{th} subgroup
N_{ra}, N_{ramin}	The neighborhood size and a minimum value of the neighborhood size
w_p	The inertia weight
S_{rnk}	The k^{th} subgroup
F_{cg}	The minimum contact force
$\boldsymbol{\delta}_{gbest}$	The optimal solution searched in the whole group
N_{sta}, N_{stamax}	The stagnation counter and a maximum value of the stagnation counter
γ_1,γ_2	Two learning factors
$\boldsymbol{u}_{r1},\boldsymbol{u}_{r2}$	Random numbers from 0 to 1

1 Introduction

Oil grooves are a key structure of heavy-duty friction pairs in large mechanical equipment, such as spindles in precision grinding machine tools, ultra-high-power hydraulic motors of tunnel boring machines, and turbines in hydropower engineering [1-4]. The primary roles of oil grooves are to store, transport, and distribute high-pressure oil throughout the whole friction pair, thereby providing the necessary hydrostatic support for friction pairs, reducing the contact force on friction pairs, as well as promoting the formation of the lubricant oil film and heat dissipation. Therefore, oil grooves have a significant effect on the load-carrying, lubrication, and wear resistance of friction pairs. Therein, the patterns (profile shape, size, and location) of oil grooves are the most critical determining factor for the performance of oil grooves [5-7]. Therefore, many researchers have carried out a large number of in-depth studies on the design and optimization of oil groove patterns, which can be broadly classified into three categories:

The first category is experience-based pattern design. Based on designers' experience, some new oil groove patterns, such as rectangle, circle, ellipse, triangle, crescent, waist-shaped hole, have been designed [8-10]; or combined patterns of the existing patterns have been designed [11-14]. Afterwards, the oil groove pattern is optimized through a large number of parameter sensitivity analyses and comparison experiments [15]. However, the above design methods are highly dependent on the designer's design experience. Even if the dimensional parameters of the initially designed pattern are optimized subsequently, the obtained pattern is only the optimal solution under the constraint of the specific initial pattern (i.e., local optimization). Therefore, this method is difficult to obtain the globally optimal oil groove pattern that is not constrained by the initial pattern.

The second category is biomimicry-based pattern design. Through in-depth analysis of biological morphology, structure, and corresponding functions, researchers have designed oil groove patterns like dragonfly wing veins [16], linden leaf veins [17], and poplar leaf veins [18]. These oil groove patterns can transport the high-pressure fluid ejected from the center hole to the entire friction pairs by the vein-like structures, so as to enhance the lubrication and oil-film support force in friction pairs. However, this design method depends heavily on the designer's keen insight. Moreover, the scale of biological structures generally differs from that of friction pairs, which means that direct imitation of a biological structure may not achieve the desired effect. Therefore, similar to the first design method, the second method is also difficult to obtain a globally optimal oil groove pattern. In addition, a lot of exploration and trial-and-error processes for different biological structures are usually required to further optimize the oil grooves, which will lead to a long design cycle.

The third category is polygon-based pattern design. Firstly, the profiles of oil grooves are parameterized and regarded as polygons, i.e., the boundaries of the oil grooves are formed by line segments. Secondly, the endpoint positions of the line segments are optimized based on various algorithms, thereby obtaining the optimal oil groove pattern. For example, some studies use x and y coordinates to define the endpoint positions of the line segments [19]. In this case, the x and y coordinates are optimized through the elite retained non-dominated sorting genetic algorithm (NSGA-II) to obtain the optimal oil groove pattern. To reduce the number of optimized variables, the endpoint positions can also be defined through a series of radial line segments with the same angular interval and start point [20]. Subsequently, the length of the radial line segments is optimized based on a genetic algorithm to obtain the optimal oil groove pattern. However, the disadvantage of this polygon-based design method is that it cannot cover all possible oil groove patterns. For example, one initial polygonal pattern is unable to form an annular pattern or hollow pattern with a blank area inside, but only a solid polygonal pattern after optimizing. If we desire to generate an annular oil groove pattern, we need to set two overlapping polygons before starting optimization. Therefore, this polygon-based design method also relies on the designer's experience and restricts the optimization algorithm's searchable range. Theoretically, it is difficult to obtain a globally optimal oil groove pattern.

For that, this study proposes the intelligent self-evolving design method for oil grooves to improve their lubrication and load-bearing capacity. Firstly, the threshold-truncated Gaussian kernel function is designed to describe oil groove patterns, realizing the unified mathematization expression of arbitrary oil groove patterns. Then, an artificial intelligence-assisted generalized pattern search algorithm (GPS+AI) is proposed, which can disturb and evolve the oil groove pattern based on the feedback contact force, thereby maximizing the load-bearing capacity of the oil groove.

The rest of this paper is organized as follows. In Section 2, the description function of oil grooves is designed, realizing a mathematical expression of any oil groove pattern. Then, the proposed artificial intelligence-assisted generalized pattern search algorithm (GPS+AI) is introduced and explained in detail in Section 3. The intelligent self-evolving design method is applied to the piston in a cam-lobe hydraulic motor. The obtained novel oil groove is presented in Section 4. In Section 5, the high-load-carrying advantage of the novel oil groove is demonstrated by comparing it with two traditional oil grooves. Finally, conclusions are given in Section 6.

2 Description function of oil groove

Before optimizing the oil groove pattern, it is necessary to establish a mathematical framework that can characterize the profiles of any oil groove pattern, i.e., to establish a generic description function. The description processing of an oil groove pattern is shown in Fig. 1. In order to ensure the universality of the proposed intelligent self-evolving design method, a complex-shaped friction pair is chosen as a case instead of the common rectangular ones. Moreover, the structure of friction pairs is generally symmetrical. Thus, the friction pair can be simplified, i.e., only a portion of the area is used to design the oil groove patterns, which can reduce computational load during the subsequent optimization process. Here, we take the 1/4 friction pair as an example, as shown in Fig. 1(c). In order to facilitate the subsequent mathematical description, the complex-shaped region of the 1/4 friction pair is mapped into a rectangular region (Fig. 1 (c) to (d)), and the rectangular region is used as the subsequent design domain. Correspondingly, the set of points $\boldsymbol{P}_{\mathrm{f}}$ (x_{fi}, y_{fi}) is transformed to the set of the anchor points $\boldsymbol{P}_{\mathrm{s}}$ (x_{si}, y_{si}) on the rectangular design domain by:

$$\begin{bmatrix} x_{si} & y_{si} \end{bmatrix} = f_{\mathrm{m}}\left(x_{fi}, y_{fi}\right) \tag{1}$$

where f_{m} is a mapping function.

In this study, the anchor points on the rectangular design domain are in the form of an equally spaced rectangular distribution. Afterward, every anchor point (P_{si}) is assigned the value φ_{si}, which can influence the shape of the oil groove as shown in Fig. 1(e)~(g). The values (φ_{si}) of the anchor points can change the controlled surface's shape, and the relationship between them is established by a Gaussian kernel function. The controlled surface is then crossed with a threshold surface to form intersecting lines, resulting in profiles of an oil groove. Accordingly, the height distribution (g_{ai}) of the controlled surface directly influences the profiles of the oil groove. The height (g_{ai}) is controlled by the values (φ_{si}) of the anchor points:

$$
\begin{aligned}
g_{ai}\left(\varphi_{si}\right) &= \sum_{si=1}^{N} w_{si} \Theta\left(\left\| P_{ai} - P_{si} \right\|_2\right) + l_0 + l_1 x_{ai} + l_2 y_{ai} \\
&= \sum_{si=1}^{N} w_{si} e^{-l_s^2 \sqrt{\left(x_{ai}-x_{si}\right)^2 + \left(y_{ai}-y_{si}\right)^2}} + l_0 + l_1 x_{ai} + l_2 y_{ai}
\end{aligned} \tag{2}
$$

where N is the total number of anchor points; Θ is the Gaussian covariance function; w_{si} is the influence weight of the anchor point P_{si}; and l_0, l_1, and l_2 are the three linear correction factors; l_s is the shape parameter, $l_s = C_r\ l_m$, C_r is a constant, and l_m is the minimum distance between the anchor points. The l_m can affect the performance of the Gaussian kernel function. An overly small l_m will lead to a sharp rise in the subsequent optimization dimensions (variables), thereby increasing the solution's time-consuming and difficulty. An overly large l_m will not be able to accurately establish every potential controlled surface. The l_m is recommended as less than 12.5% of the longest side of the rectangle domain in a study about fitting boundaries of images [21]. In this study, l_m is 10%L_d, where L_d is the longest side length of the rectangular design domain. Correspondingly, the set of anchor points ($\boldsymbol{P}_s$) contains 11×6 anchor points.

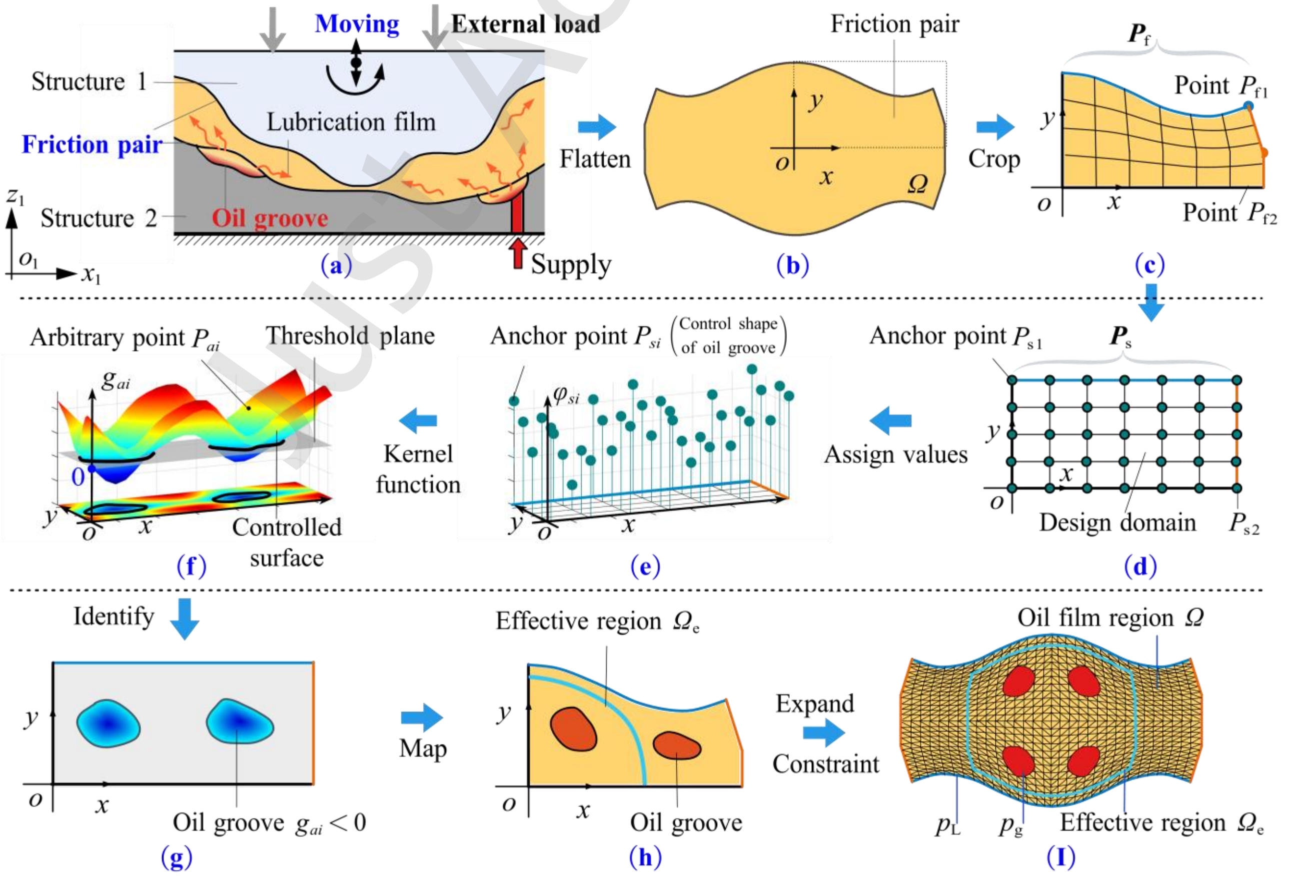

Fig. 1 The description processing of the oil groove pattern

From Eq. (2), the value (φ_{si}) of the anchor point (P_{si}) can change the height (g_{ai}) of any point on the controlled surface by the weights (w_{si}) and the three correction factors (l_0, l_1, l_2). The relationship between φ_{si} and w_{si}, l_0, l_1, l_2 is:

$$\boldsymbol{W} = \boldsymbol{H}^{-1}\boldsymbol{\varphi}_{\mathrm{s}} \tag{3}$$

where

$$\boldsymbol{W} = \begin{bmatrix} w_1 & \dots & w_N & l_0 & l_1 & l_2 \end{bmatrix}^{\mathrm{T}} \tag{4}$$

$$\boldsymbol{\varphi}_{\mathrm{s}} = \begin{bmatrix} \varphi_1 & \dots & \varphi_N & 0 & 0 & 0 \end{bmatrix}^{\mathrm{T}} \tag{5}$$

$$\boldsymbol{H} = \begin{bmatrix} \Theta_{1,1} & \cdots & \Theta_{1,N} & 1 & x_{si=1} & y_{si=1} \\ \vdots & \ddots & \vdots & \vdots & \vdots & \vdots \\ \Theta_{N,1} & \cdots & \Theta_{N,N} & 1 & x_{si=N} & y_{si=N} \\ 1 & \cdots & 1 & 0 & 0 & 0 \\ x_{si=1} & \cdots & x_{si=N} & 0 & 0 & 0 \\ y_{si=1} & \cdots & y_{si=N} & 0 & 0 & 0 \end{bmatrix} \tag{6}$$

where $\Theta_{a,b} = \Theta\left(\left\|P_{si=a} - P_{si=b}\right\|_2\right)$, denotes the Θ value of the a^{th} anchor point and the b^{th} anchor point; $x_{si=N}$ and $y_{si=N}$ denote the coordinates of the N^{th} anchor point; w_N and φ_N denote the weights and values of the N^{th} anchor point.

The solved weight ($\boldsymbol{W}$) is substituted into Eq. (2) to determine the height (g_{ai}) of the controlled surface. The controlled surface is crossed by the threshold surface that is chosen as the horizontal surface with height position 0. The intersection lines between the controlled surface and the threshold surface are the profile of the oil groove, as shown in Fig. 1(f) (g). The profile expression of the oil groove pattern is

$$G(\boldsymbol{\varphi}) = \begin{cases} \text{oil groove} & g_{ai}(\boldsymbol{\varphi}) < 0 \\ \text{oil film} & g_{ai}(\boldsymbol{\varphi}) \geq 0 \end{cases} \tag{7}$$

where $\boldsymbol{\varphi}$ is a column vector consisting of the anchor point values (φ_{si}). An oil groove pattern can be obtained by combining Eqs. (2)~(7) and solving G.

According to Eq. (7), the oil groove pattern (G) can be changed randomly by altering the anchor point values (φ). In order to get the optimal oil groove pattern, the anchor point values (φ) are optimized under the objective of minimizing the contact force of the friction pair. The mathematical expression of the optimized problem is:

$$\begin{aligned} &\text{Objective function: Min } F_{\mathrm{c}}\left(G(\boldsymbol{\varphi})\right)=\int \bar{p}_{\mathrm{c}} d\Omega \\ &\text{Constraints: } \quad \text{s.t. } \; g_{ai}=1 \quad g_{ai}\notin \Omega_{\mathrm{e}} \end{aligned} \tag{8}$$

where F_c is the contact force, Ω is the oil film region, and Ω_e is the effective region. The constraints in Eq. (8) require that the designed oil grooves appear only within the effective region (Ω_e), which ensures that the designed oil groove is usable. For example, it could limit the minimum distance between the oil groove and the friction pair boundary, ensuring enough sealing.

3 Algorithm: artificial intelligence-assisted generalized pattern search (GPS+AI)

For the optimization problem in Eq. (8), the artificial intelligence-assisted generalized pattern search (GPS+AI) algorithm is proposed, as shown in Fig. 2. Firstly, the description function of the oil groove is used to transform the initial anchor point value ($\boldsymbol{\varphi}_0$) to the initial groove pattern (G_0). The initial contact force F_{c}^{0} (objective function) is obtained by solving the lubrication model [22].

Then, the GPS algorithm (yellow area in Fig. 2) takes the anchor point value ($\boldsymbol{\varphi}^{j-1}$) of the ($j$-$1$)th iteration as a base point and creates 2N trial points in the neighborhood of the base point ($\boldsymbol{\varphi}^{j-1}$), i.e., in an N-dimensional hypersphere. The GPS algorithm then begins polling the 2N trial points ($\boldsymbol{s}_i^j$) that are converted into 2N trial oil groove patterns by the description function. The contact force (F_c) corresponding to each trial oil groove pattern is obtained by solving the lubrication model. Among them, the oil groove pattern with the smallest contact force is chosen as the solution for the jth iteration, and the corresponding anchor point value serves as the base point ($\boldsymbol{\varphi}^{j}$) for the next iteration. Subsequently, the GPS algorithm starts the (j+1)th iteration. In each iteration, every oil groove pattern and its contact force that have been polled by the GPS algorithm are stored in the database (shown as green boxes in Fig. 2).

When the recorded number of oil groove patterns is more than M_G, AI assistance (blue region in Fig. 2) is activated to generate the preferred oil groove patterns. In this study, the self-disturbing online deep learning model driven by a swarm intelligence algorithm is proposed for AI-assisted design. The basic idea of the AI-assisted design is as follows. The current optimal oil groove pattern (G_*^j) is taken as the input of the AI. Then the disturbance layer is set and disturbances are added to the input G_*^j, so as to evolve out different new oil groove patterns based on the current optimal pattern (G_*^j). The online deep learning model predicts the contact forces (F_c) of the new oil groove patterns. Meanwhile, the swarm intelligence algorithm is designed to iteratively adjust the disturbances mixed in the current optimal pattern (G_*^j) according to the predicted contact forces (F_c), so that the evolved oil groove patterns have contact forces (F_c) as small as possible.

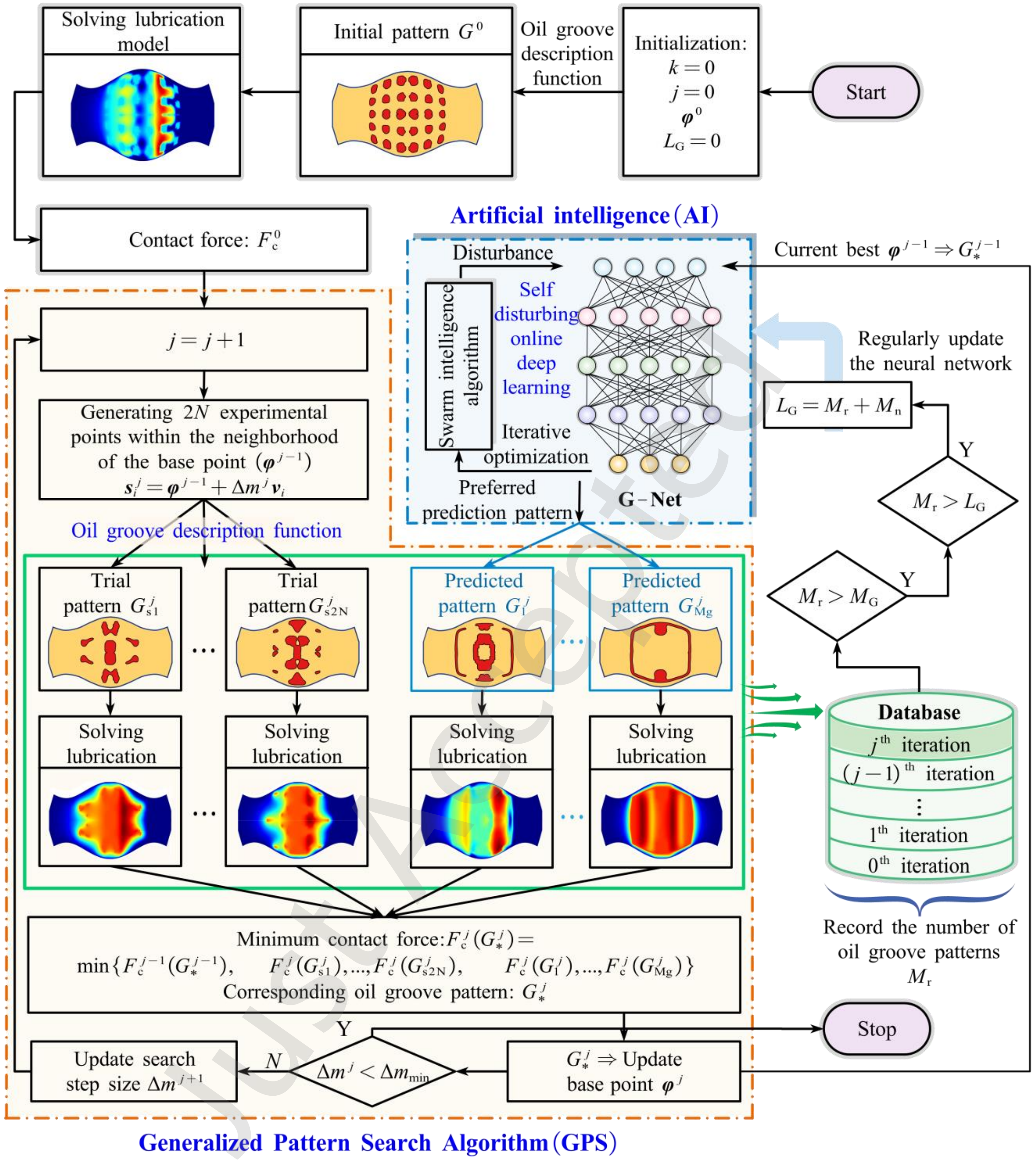

Fig. 2 Flowchart of Artificial Intelligence (AI)-Assisted Generalized Pattern Search (GPS) Algorithm

Afterward, the preferred oil groove patterns are provided to the GPS algorithm for polling and refinement. Considering that the prediction accuracy of neural networks cannot reach 100%, the AI will provide M_g preferred oil groove patterns to the GPS in each iteration (shown in the blue solid-line box in Fig. 2). In addition, as long as the number of oil grooves polled by the GPS algorithm is increased by M_{n} in the iteration process, the current self-disturbance online deep learning model is updated once. In this way, the model can learn more experience in oil groove optimization and improve the cognitive level of the model. Specific details of the GPS algorithm and AI-assisted design are as follows.

3.1 Generalized Pattern Search (GPS)

In the j^{th} iteration before the AI intervention, the GPS algorithm polls $2N$ trial points ($\boldsymbol{s}_i^j$) in the N-dimensional neighborhood of the base point ($\boldsymbol{\varphi}^{j-1}$) with the step size ($\Delta m^j$). The principle is shown in Fig. 3. It should be noted that Fig. 3 illustrates the polling principle in two dimensions (N = 2), whose principle is similar to that in N dimensions. N is the number of anchor points, and also the number of independent variables in the base point ($\boldsymbol{\varphi}$). The coordinates of the $2N$ trial points are determined by the pattern vectors $\boldsymbol{V} = [\boldsymbol{v}_1, \boldsymbol{v}_2, \ \ldots, \boldsymbol{v}_{2N}]$ and the step sizes Δm^j [23-24], which are

$$\boldsymbol{s}_i^j = \boldsymbol{\varphi}^{j-1} + \Delta m^j \boldsymbol{v}_i, \quad i = 1, 2, 3, \ldots, 2N \tag{9}$$

where $\boldsymbol{v}_i$ is an N-dimensional column vector, for i=1, 2, ..., N, the i^{th} element of $\boldsymbol{v}_i$ is 1; for i=N+1, N+2, ..., 2N, the $(i\text{-}N)^{\mathrm{th}}$ element of $\boldsymbol{v}_i$ is -1.

Then, the $2N$ trial points ($\boldsymbol{s}_i^j$) are transformed into oil groove patterns (G_{si}^j) using the description function. Next, their contact forces (F_{c}) are evaluated, i.e., the objective function values. The trial point that generates the maximum decrease in the objective function is set as the improved trial point:

$$F_{\mathrm{c}}^j\left(G_*^j(\boldsymbol{s}_*^j)\right) = \min\left\{F_{\mathrm{c}}^j\left(G_{\mathrm{s}1}^j(\boldsymbol{s}_1^j)\right), F_{\mathrm{c}}^j\left(G_{\mathrm{s}2}^j(\boldsymbol{s}_2^j)\right), \ldots, F_{\mathrm{c}}\left(G_{\mathrm{s}2N}^j(\boldsymbol{s}_{2N}^j)\right)\right\}\frac{\pi}{2} \tag{10}$$

After the AI intervenes, the right-hand side of Eq. (10) will additionally evaluate M_{g} preferred oil groove patterns from the AI. Meanwhile, the one with the smaller objective function value between the improved trial point ($\boldsymbol{s}_*^j$) and the current base point ($\boldsymbol{\varphi}^{j-1}$) is used to be the new base point ($\boldsymbol{\varphi}^j$), and the corresponding expression is:

$$\boldsymbol{\varphi}^{j}=\begin{cases}\boldsymbol{s}_{*}^{j} & F_{\mathrm{c}}^{j}\left(\boldsymbol{s}_{*}^{j}\right)\geq F_{\mathrm{c}}^{j-1}\left(\boldsymbol{\varphi}^{j-1}\right)\\ \boldsymbol{\varphi}^{j-1} & F_{\mathrm{c}}^{j}\left(\boldsymbol{s}_{*}^{j}\right)>F_{\mathrm{c}}^{j-1}\left(\boldsymbol{\varphi}^{j-1}\right)\end{cases} \tag{11}$$

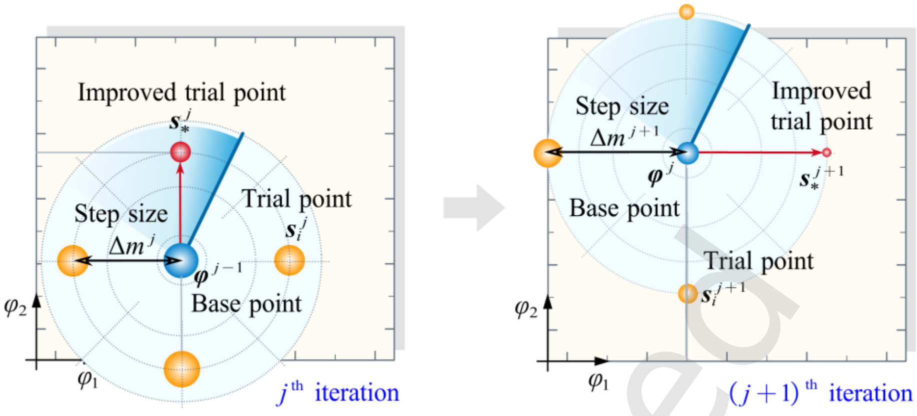

Fig. 3 Polling schematic (The size of the trial point indicates its corresponding objective function value F_{c})

When the improved trial point ($\boldsymbol{s}_{*}^{j}$) replaces the current base point ($\boldsymbol{\varphi}^{j-1}$), i.e., the first situation in Eq. (11), the step size will be enlarged ($\Delta m^{j+1}>\Delta m^{j}$), and otherwise it will be reduced ($\Delta m^{j+1}<\Delta m^{j}$). As shown in Fig. 3, in the iteration, a trial point ($\boldsymbol{s}_{*}^{j}$) with a smaller contact force (denoted by the diameter of the point) is found, and then the $(j+1)^{th}$ larger step size, $\Delta m^{j+1}>\Delta m^{j}$, will be used in the next iteration. At the same time, the variation range of the step size is restricted, i.e., $\Delta m^{j+1}\in\left[\Delta m_{\min},\Delta m_{\max}\right]$, where $\Delta m_{\min}$ and $\Delta m_{\max}$ are the lower and upper limits of the step size. The expression of the step size is:

$$\begin{gathered}\Delta m^{j+1}=\begin{cases}\kappa_{\mathrm{e}}\Delta m^{j} & F_{\mathrm{c}}^{j}\left(\boldsymbol{s}_{*}^{j}\right)\geq F_{\mathrm{c}}^{j-1}\left(\boldsymbol{\varphi}^{j-1}\right)\\ \kappa_{\mathrm{c}}\Delta m^{j} & F_{\mathrm{c}}^{j}\left(\boldsymbol{s}_{*}^{j}\right)>F_{\mathrm{c}}^{j-1}\left(\boldsymbol{\varphi}^{j-1}\right)\end{cases}\\ \Delta m^{j+1}=\min\left(\max\left(\Delta m_{\min},\Delta m^{j+1}\right),\ \Delta m_{\max}\right)\end{gathered} \tag{12}$$

where $\kappa_{\mathrm{e}}>1$ and $0<\kappa_{\mathrm{c}}<1$ are the expansion and contraction factors of the step size, respectively. When the step size reaches the lower limit, i.e., $\Delta m^{j}\geq\Delta m_{\min}$, the iteration terminates.

After that, the GPS algorithm again polls the $2N$ trial points in the neighborhood of the new base point ($\boldsymbol{\varphi}^{j}$) using the updated step size and repeats the above process. The above update of the base point can make the new oil groove pattern closer to the optimal solution, thereby generating higher-quality data samples for updating the AI. The final purpose is to improve the confidence level of oil groove patterns generated by the AI.

When there are more than M_G oil groove patterns (G_{si}^j) polled by the GPS algorithm, the AI is activated. In this study, M_G =600, Δm_{min} =10^{-3}, M_n= 100, M_g =5. The AI generates the preferred oil groove patterns through the proposed self-disturbing online deep learning governed by the swarm intelligence algorithm. These preferred oil groove patterns are provided to the GPS algorithm for evaluation and refinement. The specific process of the AI is as follows.

3.2 AI: self-disturbing online deep learning

Self-disturbing represents that a disturbance term is actively mixed into the inputs of the deep learning model to evolve new oil groove patterns. Meanwhile, the disturbance term can be iteratively self-adjusted based on the swarm intelligence algorithm. Online means online learning, which represents the process of learning and upgrading the model batch by batch on new “data streams” generated with iterations, rather than completing the model training by one offline learning [25-26]. Therefore, we don't need to prepare training samples for AI in advance. Deep learning model specifically uses a kind of convolutional neural network, G-Net, which is designed based on the characteristics of the oil groove pattern, as shown in Fig. 4.

In detail, the G-Net contains one disturbance layer, four convolutional layers, one pooling layer, and three fully connected layers. The disturbance layer is designed to realize the mutation of oil groove patterns. In addition, the last fully connected layer of the G-Net is directly used to output the contact force (F_c) of the corresponding oil groove patterns. This is different from conventional CNN, which usually uses SoftMax or Sigmoid for classification (discrete quantities) after fully connected layers [27].

Additionally, large-sized convolutional kernels, such as 11×11 and 7×7, are used in the G-Net convolutional layers C1, C2, and C3. However, many current convolutional neural networks tend to choose the depth structure with multiple small-sized (e.g., 3 × 3) convolutional kernel stacks [28-30], so as to reduce network parameters and computation. The reason for choosing the large convolution kernels in this study is that they have a large effective receptive field, that is, a wide viewing range [31]. In the whole oil groove pattern, the proportion of the oil groove region is relatively small, making it difficult for the small convolutional kernel to capture the key features of the oil groove region. For this reason, a large convolutional kernel is chosen in the designed G-Net. In addition, the edges of the input image are padded with 0 during the convolution process in layers C1 and C2, which can preserve the critical information on the input image boundary.

To reduce the input dimension and training difficulty of the G-Net network, the input images, i.e., the oil groove patterns, are preprocessed, as shown in Fig. 4. Considering the symmetry of the oil groove pattern as well as the fact that the oil grooves only appear in the effective region (Ω_e), the 1/4 effective region (Ω_e) is cropped for the input of the G-Net network. To facilitate the subsequent processing, the 1/4 effective region (Ω_e) is then mapped as a rectangular region, corresponding to Fig. 1 (g). Then the rectangular region is divided into individual pixel blocks. Among them, the pixel blocks whose centers are covered by oil grooves are assigned a value of 1, and the rest are 0. This process achieves the dual purpose of input normalization and distinguishing between oil groove/oil film regions. The matrix of the pixelated oil groove pattern $\boldsymbol{G}_\mathrm{p} \in \mathbb{R}^{H_\mathrm{G} \times W_\mathrm{G} \times D_\mathrm{G}}$ is passed to G-Net for feature extraction and prediction of contact force (F_c).

During the G-Net training stage, the disturbances need to be set to a constant 0 to enable the model to accurately learn the nonlinear mapping relationship between the oil groove pattern and the contact force (F_c). After the training is completed, the current optimal solution $G_*^{j-1}\left(\boldsymbol{\varphi}^{j-1}\right)$ is used as the input. Then a group of disturbances $\boldsymbol{\delta}^i = \left[\boldsymbol{\delta}_1^i,\ \boldsymbol{\delta}_2^i,\ ...,\ \boldsymbol{\delta}_k^i,\ ...,\ \boldsymbol{\delta}_{N_\mathrm{r}}^i\right]$ is randomly generated, each of which $\boldsymbol{\delta}_k^i \in \mathbb{R}^{N\times 1}$ is an N-dimensional vector. Each disturbance is added to the input, and multiple (N_r) new oil groove patterns are evolved based on the current optimal solution:

$$G_{\mathrm{p}}\left(\varphi^{j-1}+\delta^{i}\right)=\left[G_{\mathrm{p}1}\left(\varphi^{j-1}+\delta_{1}^{i}\right),\ G_{\mathrm{p}2}\left(\varphi^{j-1}+\delta_{2}^{i}\right),\ldots,\ G_{\mathrm{p}N_{\mathrm{r}}}\left(\varphi^{j-1}+\delta_{N_{\mathrm{r}}}^{i}\right)\right] \tag{13}$$

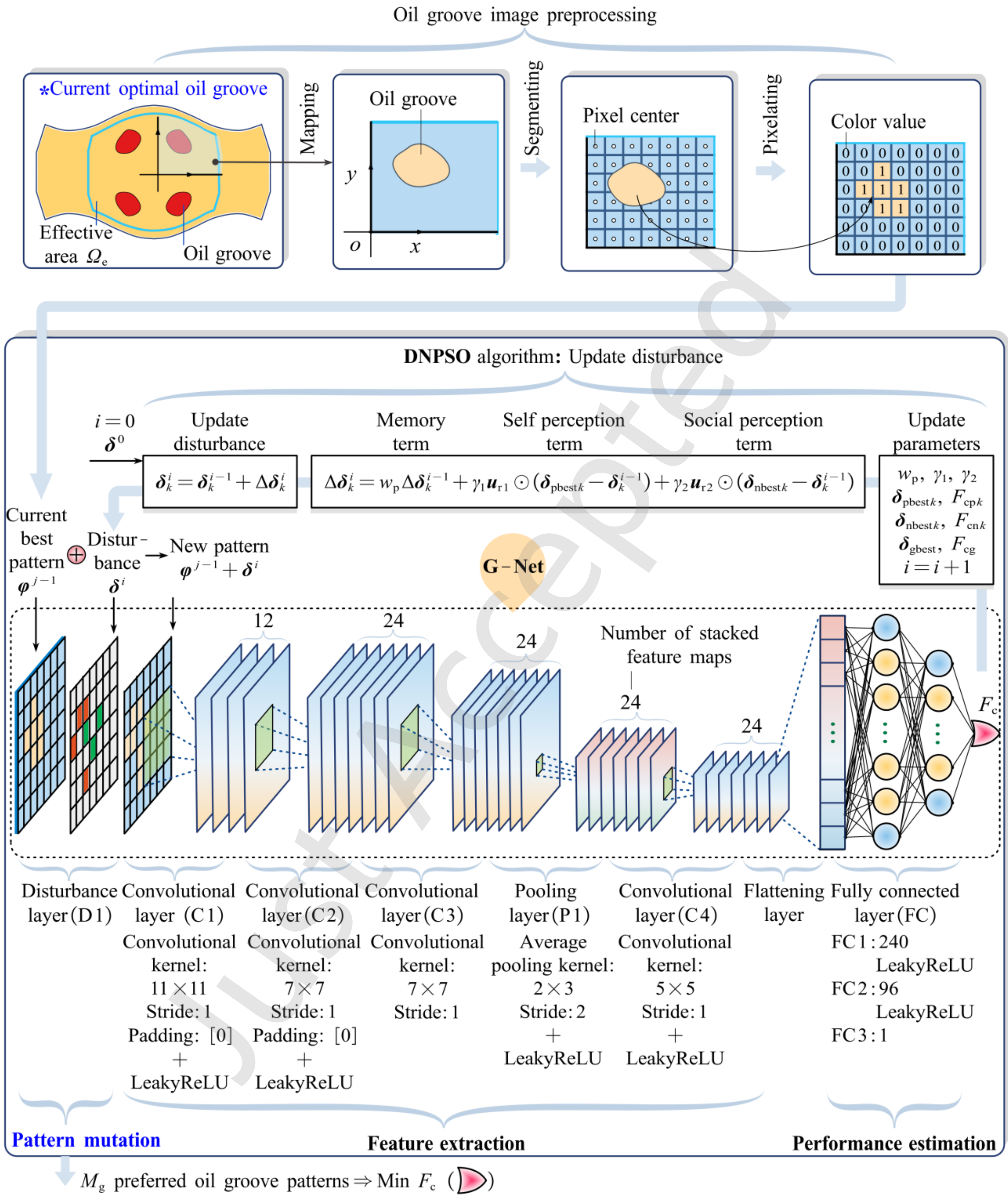

Fig. 4 Schematic of self-disturbing online deep learning

Afterward, these new oil groove patterns are pixelized, and as the inputs (G_{p}), they are first padded, convolved, and nonlinearized in the C1 layer of the G-Net. The padding with 0 avoids the loss of oil groove information at the edge of the image. The image is symmetrically padded at top/bottom and left/right, and the height and width dimensions of the image are increased by

$$L_{\mathrm{H}} = \left\lfloor \left(\left\lceil \frac{H_{\mathrm{G}}}{H_{\mathrm{s}}} \right\rceil - 1 \right) H_{\mathrm{s}} + H_{\mathrm{k}} - H_{\mathrm{G}} \right\rfloor \tag{14}$$

$$L_{\mathrm{W}} = \left\lfloor \left(\left\lceil \frac{W_{\mathrm{G}}}{W_{\mathrm{s}}} \right\rceil - 1 \right) W_{\mathrm{s}} + W_{\mathrm{k}} - W_{\mathrm{G}} \right\rfloor \tag{15}$$

where L_{H} and L_{W} are the increased height and width of the image after padding, respectively; H_{G}, W_{G}, and D_{G} are the height, width, and depth (number of channels) of the input image (i.e., oil groove pattern); H_{s} and W_{s} are the step size of the convolution kernel moving along the direction of height and width; and H_{k} and W_{k} are the height and width of the convolution kernel. The padding image is used as the input to the convolution operation $\boldsymbol{I}_{\mathrm{c}} \in \mathbb{R}^{H_{\mathrm{I}} \times W_{\mathrm{I}} \times D_{\mathrm{I}}}$. The output feature map after convolution is

$$\boldsymbol{X}_{\mathrm{c}}^{kc}(i,j) = \left(\boldsymbol{I}_{\mathrm{c}} * \boldsymbol{K}_{\mathrm{c}}\right)_{i,j} = \sum_{m=0}^{H_{\mathrm{k}}-1} \sum_{n=0}^{W_{\mathrm{k}}-1} \sum_{d=1}^{D_{\mathrm{I}}} \boldsymbol{K}_{\mathrm{c}}^{m+1,\, n+1,\, d} \boldsymbol{I}_{\mathrm{c}}^{i+m+(i-1)H_{\mathrm{s}},\, j+n+(j-1)W_{\mathrm{s}},\, d} + b^{kc} \tag{16}$$

where k_{c} denotes the $k_{\mathrm{c}}^{\mathrm{th}}$ convolution kernel of the current layer; $\boldsymbol{X}_{\mathrm{c}}^{kc}(i,j)$ denotes the element of the i^{th} row and j^{th} column in the feature map ($\boldsymbol{X}_{\mathrm{c}}$) from the $k_{\mathrm{c}}^{\mathrm{th}}$ convolution kernel; * is the convolution operator; H_{I}, W_{I}, and D_{I} are the height, width, and depth of the input image ($\boldsymbol{I}_{\mathrm{c}}$); $\boldsymbol{I}_{\mathrm{c}}^{i+m+(i-1)H_{\mathrm{s}}, j+n+(j-1)W_{\mathrm{s}}, d}$ denotes the element from the $i+m+(i-1)\ H_{\mathrm{s}}$ row, $j+n+(j-1)\ W_{\mathrm{s}}$ column, d channel of the $\boldsymbol{I}_{\mathrm{c}}$; $\boldsymbol{K}_{\mathrm{c}} \in \mathbb{R}^{H_{\mathrm{k}} \times W_{\mathrm{k}} \times D_{\mathrm{I}}}$ is the convolution kernel (weight matrix); $\boldsymbol{K}_{\mathrm{c}}^{m+1,n+1,d}$ denotes the element from the m+1 row, n+1 column, and d channel of the $\boldsymbol{K}_{\mathrm{c}}$; b^{kc} is the bias of the $k_{\mathrm{c}}^{\mathrm{th}}$ convolution kernel. The feature map ($\boldsymbol{X}_{\mathrm{c}}$) generated by the above convolution operation is nonlinearized by the activation function LeakyReLU (σ_{L}) to obtain the output ($\boldsymbol{Y}_{\mathrm{c1}}$) of the C1 layer:

$$\boldsymbol{Y}_{\mathrm{c1}} = \sigma_{\mathrm{L}}\left(\boldsymbol{X}_{\mathrm{c}}\right) \tag{17}$$

$$\sigma_{\mathrm{L}}(x) = \begin{cases} x & x \geq 0 \\ a_{\mathrm{L}} x & x < 0 \end{cases}, \quad a_{\mathrm{L}} \in (0, 1) \tag{18}$$

where a_{L} is the parameter of the activation function.

The subsequent convolution operations of the layers C2, C3, and C4 are similar to those described above, and will not be repeated. The pooling layer P1 after the layer C3 is essentially a downsampling process, which eliminates "low-value" pixels and reduces the size of the image. The average pooling layer P1 is defined as:

$$\boldsymbol{X}_{\mathrm{c3}}^{d}\left(i,j\right)=\frac{\sum_{m=0}^{H_{\mathrm{p}}-1}\sum_{n=0}^{W_{\mathrm{p}}-1}\boldsymbol{Y}_{\mathrm{c3}}^{i+m+(i-1)H_{\mathrm{s}},\, j+n+(j-1)W_{\mathrm{s}},\, d}}{H_{\mathrm{p}}W_{\mathrm{p}}} \tag{19}$$

where $\boldsymbol{Y}_{\mathrm{c3}}$ is the feature map output from the C3 layer; H_{p} and W_{p} are the height and width of the pooling kernel; and the meanings of the other parameters are the same as in Eqs. (14)(15).

The feature map output from the C4 layer is converted to a column vector ($\boldsymbol{X}_{\mathrm{F}}$), then passes through three fully connected layers and outputs the contact force (F_{c}). The corresponding expression is

$$F_{\mathrm{c}}=\boldsymbol{K}_{\mathrm{f3}}\left\{\sigma_{\mathrm{L}}\left(\boldsymbol{K}_{\mathrm{f2}}\left\{\sigma_{\mathrm{L}}\left(\boldsymbol{K}_{\mathrm{f1}}\boldsymbol{X}_{\mathrm{F}}+\boldsymbol{b}_{\mathrm{f1}}\right)\right\}+\boldsymbol{b}_{\mathrm{f2}}\right)\right\}+\boldsymbol{b}_{\mathrm{f3}} \tag{20}$$

where $\boldsymbol{K}_{\mathrm{f1}}$, $\boldsymbol{K}_{\mathrm{f2}}$ and $\boldsymbol{K}_{\mathrm{f3}}$ are the weights of the three-layer fully connected layers; $\boldsymbol{b}_{\mathrm{f1}}$, $\boldsymbol{b}_{\mathrm{f2}}$, and $\boldsymbol{b}_{\mathrm{f3}}$ are the biases of the three-layer fully connected layers.

The contact force (F_{c}) output from the G-Net is fed to the swarm intelligence algorithm, specifically the Dynamic Neighborhood Particle Swarm Algorithm (DNPSO), which is a modified version of the Particle Swarm Algorithm [32,33], and its pseudo-code is shown in Fig. 5. The DNPSO calculates the optimal solution in a random subgroup ($\boldsymbol{\delta}_{\mathrm{nbest}k}$) in each iteration, rather than the optimal solution in the entire group ($\boldsymbol{\delta}_{\mathrm{gbest}}$) in the Particle Swarm Algorithm. Each disturbance ($\boldsymbol{\delta}_k^i$) is regarded as an individual and corresponds to a mutated oil groove pattern. All disturbances form a group ($\boldsymbol{\delta}^i$) including N_{r} oil groove patterns. Subsequently, the G-net evaluates the contact forces of the group ($\boldsymbol{\delta}^i$) (as shown in line 15 of Fig. 5).

If the k^{th} disturbance ($\boldsymbol{\delta}_k^i$) generates the oil groove whose contact force $F_{\mathrm{c}}\left(\boldsymbol{\delta}_k^i\right)$ satisfies

$F_{\mathrm{c}}\left(\boldsymbol{\delta}_k^i\right) < F_{\mathrm{cp}k}$, then we let $F_{\mathrm{cp}k} = F_{\mathrm{c}}\left(\boldsymbol{\delta}_k^i\right)$, $\boldsymbol{\delta}_{\mathrm{pbest}k} = \boldsymbol{\delta}_k^i$, as shown in line 16 in Fig. 5. The $F_{\mathrm{cp}k}$ is the minimum contact force found by the k^{th} individual up to now, and $\boldsymbol{\delta}_{\mathrm{pbest}k}$ is the current optimal disturbance, i.e., the optimal solution currently searched by individuals.

Subsequently, random N_{ra} disturbances form the k^{th} subgroup (S_{rnk}) in the neighborhood of the disturbance ($\boldsymbol{\delta}_k^i$), as shown in lines 18-19 in Fig. 5. The disturbance ($\boldsymbol{\delta}_{*k}^i$) has a minimum contact force (F_{c}) in the subgroup (S_{rnk}). Thus, let $\boldsymbol{\delta}_{\mathrm{nbest}k} = \boldsymbol{\delta}_{*k}^i$, $F_{\mathrm{cn}k} = F_{\mathrm{c}}\left(\boldsymbol{\delta}_{*k}^i\right) = \min\left\{F_{\mathrm{c}}\left(S_{\mathrm{rn}k}\right)\right\}$. The F_{cnk} and $\boldsymbol{\delta}_{\mathrm{nbest}k}$ denote the minimum contact force and the optimal solution searched in the k^{th} subgroup, respectively. Among them, the disturbance ($\boldsymbol{\delta}_*^i$) is identified, which minimizes contact force (F_{c}) in the whole group, as shown in line 22 in Fig. 5. Then let $F_{\mathrm{cg}} = F_{\mathrm{c}}\left(\boldsymbol{\delta}_*^i\right) = \min\left\{F_{\mathrm{cn}k}\right\}$ and $\boldsymbol{\delta}_{\mathrm{gbest}}^i = \boldsymbol{\delta}_*^i$. The F_{cg} and $\boldsymbol{\delta}_{\mathrm{gbest}}$ denote the minimum contact force and the optimal solution searched in the whole group, respectively.

If the contact force (F_{cg}) is not reduced compared to the previous iteration, the neighborhood size (N_{ra}) is expanded, and the stagnation counter (N_{sta}) is increased by 1. Otherwise, the neighborhood size (N_{ra}) is set to a minimum value (N_{ramin}), and the stagnation counter (N_{sta}) is decreased by 1; Meanwhile, the inertia weights (w_{p}) are updated. The details are shown in Fig. 5, lines 23 to 30.

If the iteration reaches the maximum value (N_{pmax}) or the stagnation counter (N_{sta}) reaches the maximum value (N_{stamax}), the iteration will be stopped. Otherwise, it goes to the next iteration. In the next iteration, the disturbance is redefined based on the optimal solution δ_{pbestk} and δ_{nbestk} found by each individual and its neighborhood (line 14 in Fig. 5):

$$\Delta\boldsymbol{\delta}_k^i = w_{\mathrm{p}}\Delta\boldsymbol{\delta}_k^{i-1} + \gamma_1 \boldsymbol{u}_{\mathrm{r1}} \mathrm{e} \left(\boldsymbol{\delta}_{\mathrm{pbest}k} - \boldsymbol{\delta}_k^{i-1}\right) + \gamma_2 \boldsymbol{u}_{\mathrm{r2}} \mathrm{e} \left(\boldsymbol{\delta}_{\mathrm{nbest}k} - \boldsymbol{\delta}_k^{i-1}\right) \tag{21}$$

$$\boldsymbol{\delta}_k^i = \boldsymbol{\delta}_k^{i-1} + \Delta\boldsymbol{\delta}_k^i \tag{22}$$

where γ_1 and γ_2 are two learning factors; $\boldsymbol{u}_{\mathrm{r1}}$ and $\boldsymbol{u}_{\mathrm{r2}}$ are random numbers from 0 to 1, which serve to increase the randomness.

When the iteration ends, the optimal disturbance ($\boldsymbol{\delta}_{\text{gbest}}$) in the whole group is added into the current optimal oil groove pattern, evolving a new and perhaps better oil groove pattern. Considering that the prediction accuracy of neural networks cannot reach 100%, the above AI will be run M_g times to mutate out M_g preferred oil groove patterns. These patterns will be provided to the GPS algorithm for lubrication analysis, as shown in the blue solid box in Fig. 3.

DNPSO algorithm**:** Adjust disturbance $\boldsymbol{\delta}$ to predict optimal oil groove

Initialization

Set $w_p, w_{\text{pmin}}, w_{\text{pmax}}, \gamma_1, \gamma_2, N_{\text{pmax}}, \varepsilon_g, N_r, N_{\text{ra}}, N_{\text{ramin}} = \lfloor 0.25 N_r \rfloor, N_{\text{sta}}, N_{\text{stamax}}$

Randomly create $\boldsymbol{\delta}^0$ within $[\delta_{\min}, \delta_{\max}]$, which contains N_r disturbance vectors

Predict contact force: $(\boldsymbol{\varphi}^{j-1} + \boldsymbol{\delta}_k^0) \Rightarrow \overbrace{\text{G} - \text{Net}} \Rightarrow F_c(\boldsymbol{\delta}_k^0)$

$F_{\text{cp}k} = F_c(\boldsymbol{\delta}_k^0), \boldsymbol{\delta}_{\text{pbest}k} = \boldsymbol{\delta}_k^0,\ F_{\text{cg}} = F_c(\boldsymbol{\delta}_*^0) = \min\{F_{\text{cp}k}\},\ \boldsymbol{\delta}_{\text{gbest}} = \boldsymbol{\delta}_*^0;$

Randomly choose N_{ra} disturbance to form a subgroup ($S_{\text{rn}k}$), which contains the k^{th} disturbance ($\boldsymbol{\delta}_k^0$)

$F_{\text{cs}k} = F_c((\boldsymbol{\delta}_{*k}^0)) = \min\{F_c(S_{\text{rn}k})\},\ \boldsymbol{\delta}_{\text{nbest}k} = \boldsymbol{\delta}_{*k}^0$

Randomly and uniformly create $\Delta\boldsymbol{\delta}^0$ within $[\Delta\delta_{\min}, \Delta\delta_{\max}]$, which contains N_r disturbance increment vectors

$i = 1$

repeat

for $k = 1$ **to** N_r **do**

Update disturbance:

$\boldsymbol{u}_{r1}, \boldsymbol{u}_{r2} \in \mathbb{R}^{N \times 1}$ is a random number uniformly distributed within $(0, 1)$

$\Delta\boldsymbol{\delta}_k^i = w_p \Delta\boldsymbol{\delta}_k^{i-1} + \gamma_1 \boldsymbol{u}_{r1} \odot (\boldsymbol{\delta}_{\text{pbest}k} - \boldsymbol{\delta}_k^{i-1}) + \gamma_2 \boldsymbol{u}_{r2} \odot (\boldsymbol{\delta}_{\text{nbest}k} - \boldsymbol{\delta}_k^{i-1}) \ \Rightarrow\ \boldsymbol{\delta}_k^i = \boldsymbol{\delta}_k^{i-1} + \Delta\boldsymbol{\delta}_k^i$

Predict contact force: $(\boldsymbol{\varphi}^{j-1} + \boldsymbol{\delta}_k^i) \Rightarrow \overbrace{\text{G} - \text{Net}} \Rightarrow F_c(\boldsymbol{\delta}_k^i)$

Update individual optimal solution: $\boldsymbol{\delta}_{\text{pbest}k} = \begin{cases} \boldsymbol{\delta}_{\text{pbest}k} & F_c(\boldsymbol{\delta}_k^i) \geq F_{\text{cp}k} \\ \boldsymbol{\delta}_k^i & F_c(\boldsymbol{\delta}_k^i) < F_{\text{cp}k} \end{cases},\quad F_{\text{cp}k} = \begin{cases} F_{\text{cp}k} & F_c(\boldsymbol{\delta}_k^i) \geq F_{\text{cp}k} \\ F_c(\boldsymbol{\delta}_k^i) & F_c(\boldsymbol{\delta}_k^i) < F_{\text{cp}k} \end{cases}$

Update the optimal solution within the random neighborhood of an individual:

Randomly choose N_{ra} disturbance to form a subgroup ($S_{\text{rn}k}$), which contains the k^{th} disturbance ($\boldsymbol{\delta}_k^i$)

$F_{\text{cn}k} = F_c(\boldsymbol{\delta}_{*k}^i) = \min\{F_c(S_{\text{rn}k})\},\ \boldsymbol{\delta}_{\text{nbest}k} = \boldsymbol{\delta}_{*k}^i$

end for

Update mark of the optimal oil groove: $G_{\text{mark}} = \begin{cases} \text{true} & \min\{F_{\text{cn}k}\} < F_{\text{cg}} \\ \text{false} & \min\{F_{\text{cn}k}\} \geq F_{\text{cg}} \end{cases}$

Update the optimal solution for the group: $F_{\text{cg}} = F_c(\boldsymbol{\delta}_*^i) = \min\{F_{\text{cn}k}\},\quad \boldsymbol{\delta}_{\text{gbest}} = \boldsymbol{\delta}_*^i$

if $G_{\text{mark}} = \text{true}$

Count for stagnation: $N_{\text{sta}} = \max(0, N_{\text{sta}} - 1)$

Reduce Neighborhood: $N_{\text{ra}} = N_{\text{ramin}}$

Update inertia weight: $w_p = \begin{cases} 2w_p & N_{\text{sta}} < 2 \\ 0.5w_p & N_{\text{sta}} > 5 \end{cases},\quad w_p = \max(\min(w_{\text{pmax}}, w_p), w_{\text{pmin}})$

else

Count for stagnation: $N_{\text{sta}} = N_{\text{sta}} + 1$

Expand Neighborhood: $N_{\text{ra}} = \min(N_{\text{ra}} + N_{\text{ramin}}, N_r)$

end if

$i = i + 1$

until $(i \leq N_{\text{pmax}})$ **or** $(N_{\text{sta}} = N_{\text{stamax}})$

Output: a preferred oil groove: $(\boldsymbol{\varphi}^{j-1} + \boldsymbol{\delta}_{\text{gbest}}) \Rightarrow G_m^j$

Fig. 5 Pseudo-code of the Dynamic Neighborhood Particle Swarm Algorithm (DNPSO)

4 Optimal Oil Groove Patterns

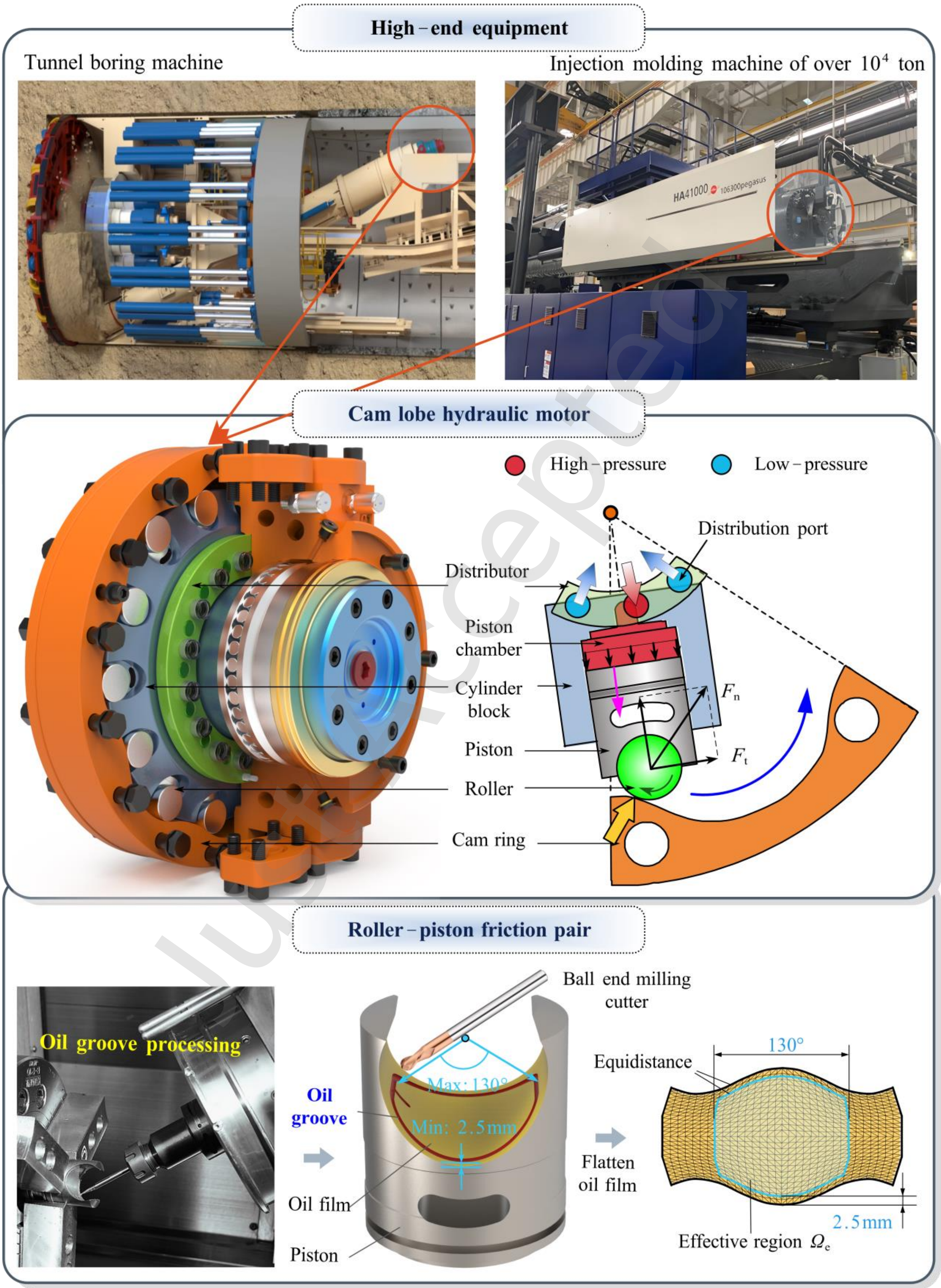

Fig. 6 Oil groove on piston in CRM-HA 50 cam-lobe hydraulic motor and design constraints

As an example, the oil groove in a CRM-HA 50 cam lobe hydraulic motor is designed, as shown in Fig. 6. The cam lobe hydraulic motor is composed of pistons, rollers, a cam ring, a cylinder block, etc. During running, high-pressure oil periodically enters the bottom of the pistons, pressing the pistons and rollers to move along the slope of the cam ring, thereby driving the motor to rotate and output torque.

Meanwhile, the cam ring exerts a reactive force (F_n) on the rollers, causing the rollers and pistons to slide relatively under heavy load. In order to extend the service life of the roller-piston friction pair and reduce the friction force, an oil groove is set inside the roller-piston friction pair.

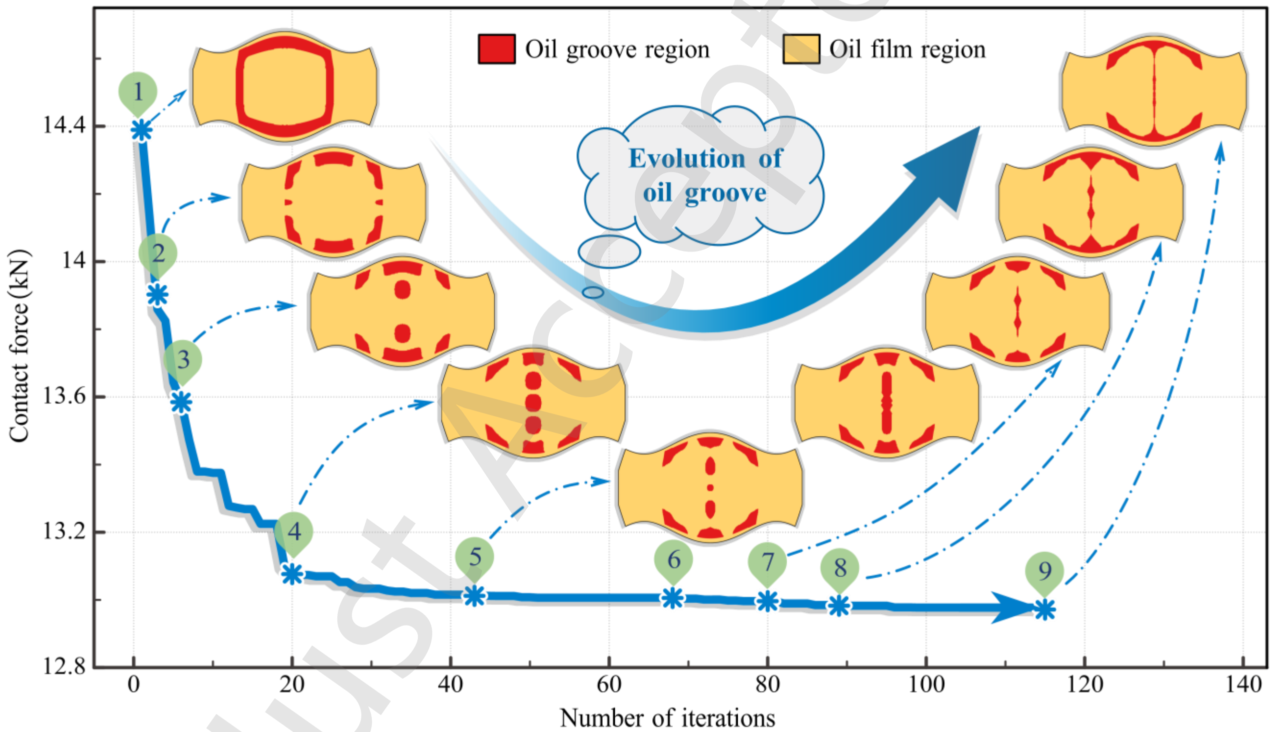

Fig. 2 The evolution of the oil groove pattern

The oil groove is located on the inner cylindrical surface of the piston. The high-pressure oil from the bottom of the piston can flow upward into the oil groove through the channel inside the piston, and be transported to the friction pair through the oil groove, providing lubrication and hydrostatic support for the roller-piston friction pair. This friction pair is flattened and presented in the right subplot of Fig. 6. In this case, the constraint during design, i.e., the effective region (Ω_e) in Eq. (8), is set to ensure that the designed oil groove is usable, as shown in Fig. 6. On the one hand, it limits the left and right spans of the oil groove to not more than 130°, ensuring that its left and right boundaries are machinable. On the other hand, it limits the minimum distance between the oil groove and the friction pair to 2.5 mm, ensuring enough sealing.

During design, the evolution of the objective function, i.e., contact force (F_c), and the corresponding oil groove patterns are shown in Fig. 7. As the iteration proceeds, the oil groove pattern gradually evolves into a curved side H-shape, as shown in the No. 9 pattern in Fig. 7.

In order to verify the feasibility of the proposed design method and the obtained optimal oil groove pattern, the No.9 oil groove pattern in Fig. 7 is manufactured. Meanwhile, the oil groove pattern is moderately simplified to reduce the difficulty of oil groove machining. The final oil groove is shown in Fig. 8. The oil grooves currently used by the two main motor manufacturers, i.e., the traditional oil grooves, are chosen as comparisons, as shown in Fig. 8. The oil grooves currently used by the two main motor manufacturers, i.e., the traditional oil grooves, are chosen as comparisons, as shown in Fig. 8. These traditional oil grooves represent the prevalent industry practice. Their patterns are initially conceived based on empirical knowledge, followed by parametric optimization to refine dimensions. As such, they exemplify the experience-based and parameter-optimized design approach, serving as established references against which the performance of the newly proposed self-evolving design method is evaluated.

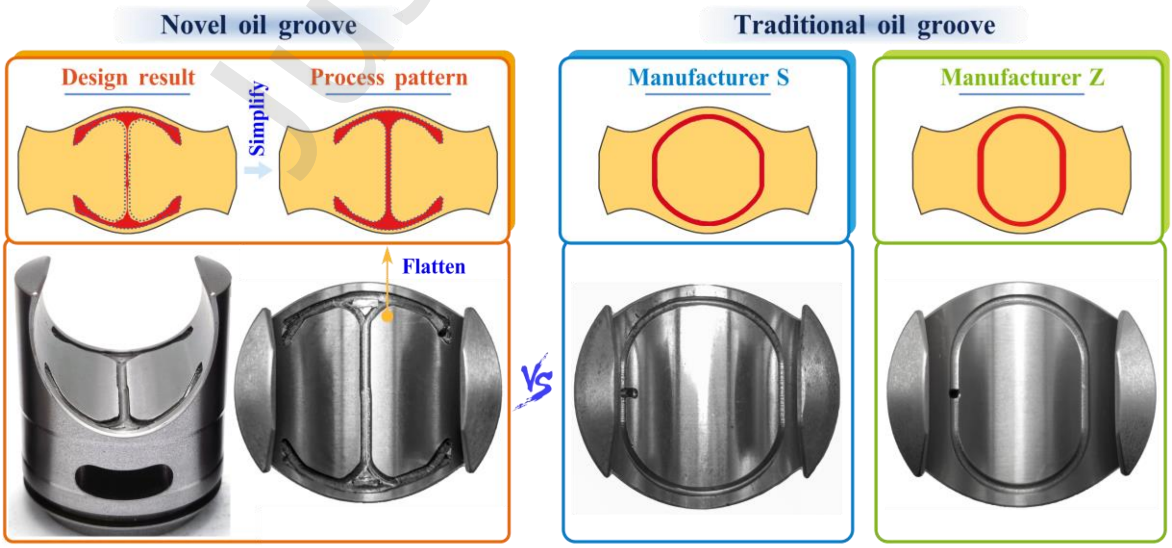

Fig. 3 Novel oil groove and traditional oil grooves

5 Experimental validation and result analysis

The validation is carried out on the developed quasi-actual testing rig for the roller-piston friction pair [34]. The principle and structure of the quasi-actual testing rig are shown in Fig. 9. The testing rig employs a drive shaft to replace the cam ring in the motor. The drive shaft can provide reactive force and driving speed for the roller, and the bottom of the piston is supplied with high-pressure oil, thereby simulating the working state between the roller and piston. Considering that the load-carrying capacity of the oil groove affects the friction of the roller-piston pair, this study uses the measured friction torque of the roller-piston pair to evaluate the load-bearing capacity of the oil groove. A total of eight pressure groups of 1, 5, 10, 15, 20, 25, 30, and 35 MPa are tested, while the equivalent motor speed is linearly increased from 0.5 rpm to 33 rpm. During the test, 46# anti-wear hydraulic oil is supplied at the bottom of the piston, and the initial oil temperatures for the different tests are 15℃~19℃. The measured friction torques of the roller-piston pairs are shown in Fig. 10.

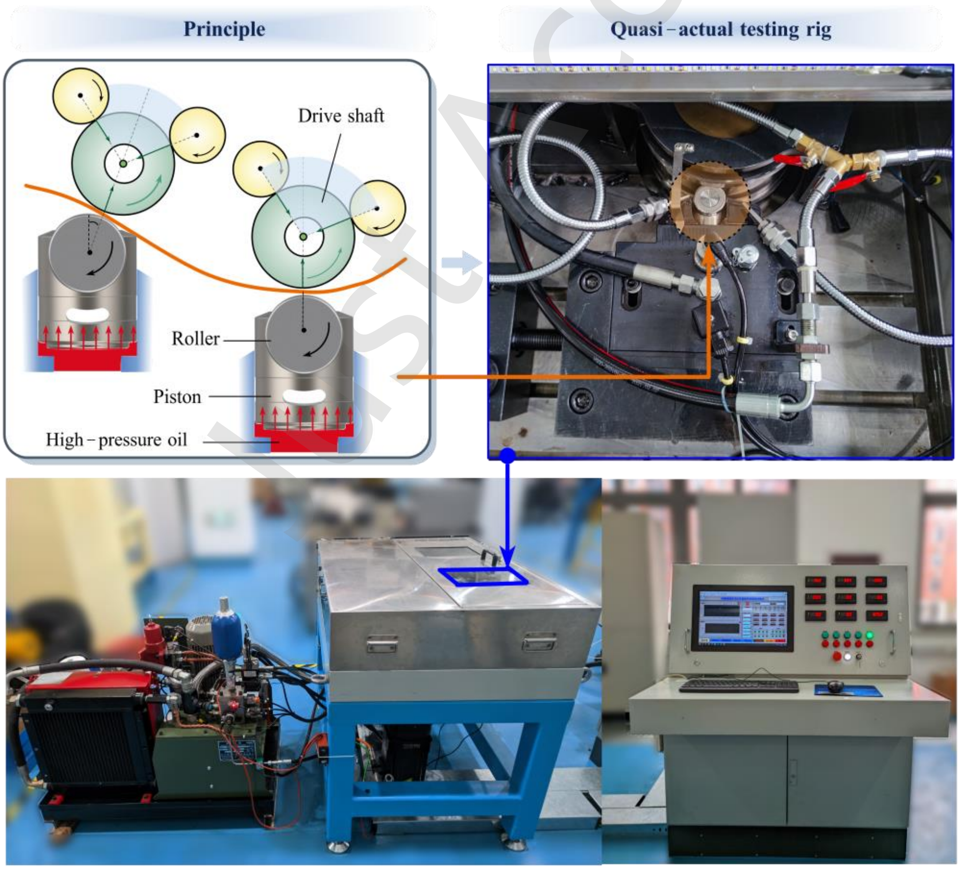

Fig. 4 Quasi-actual testing rig of roller-piston friction pair

According to Fig. 10(b), the friction torque of the novel groove is significantly lower than that of the other two traditional grooves at different pressures. At 35 MPa and 0.5 rpm, the new groove reduces the friction torque by 16% and 28%, respectively, compared with the other two conventional grooves. At 35 MPa and 33 rpm, the new groove reduces the friction torque of the roller-piston pair by 88% and 63%, respectively.

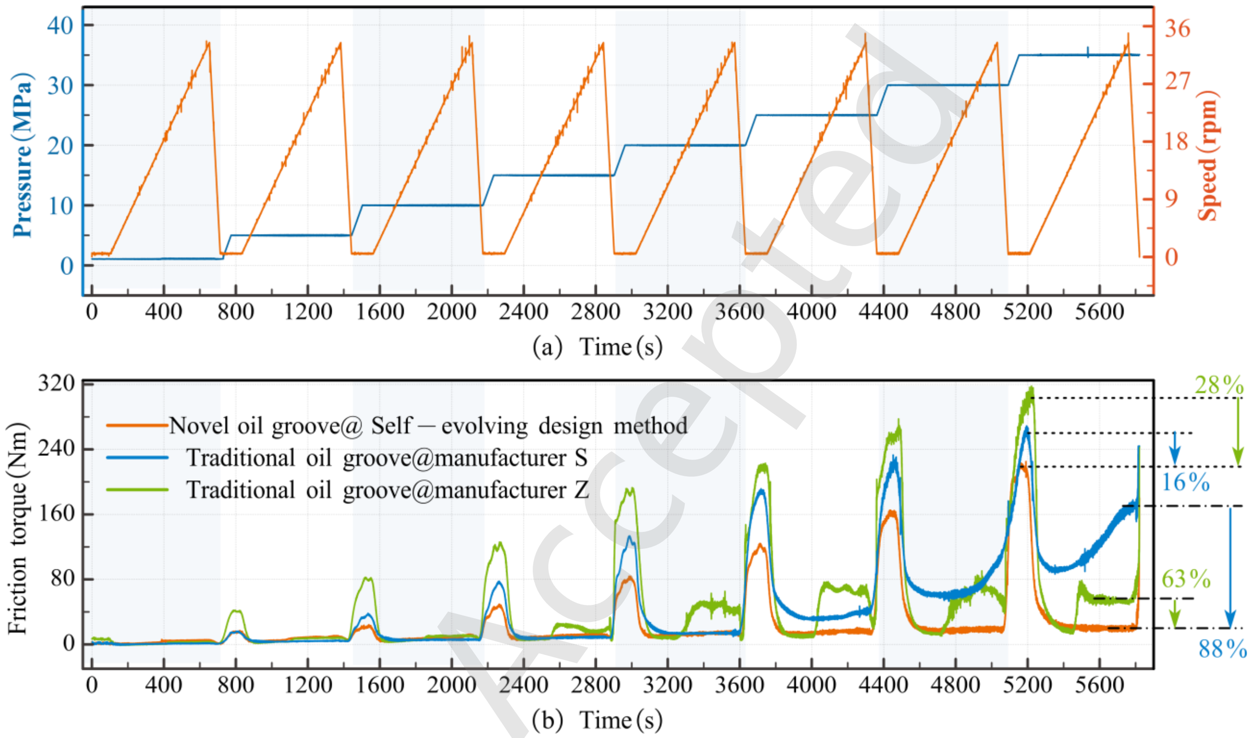

Fig. 10 The measured friction torques of the roller-piston pairs

6 Conclusion

In order to improve the load-carrying capacity of the oil groove, this study proposes an AI-assisted self-evolving design method of oil grooves. By designing the threshold-truncated Gaussian kernel function to define the profiles of oil groove patterns, any oil groove pattern can be uniformly expressed by a mathematical expression. Then, the AI-assisted generalized pattern search algorithm (GPS+AI) is proposed to design the oil groove pattern and evolve it towards minimizing contact force (maximizing load-bearing capacity). Therein, the GPS algorithm is responsible for searching and adjusting the oil groove during the initial iteration, and determining whether the iteration should be terminated. AI is designed as the self-disturbing online deep learning driven by the swarm intelligence algorithm. It utilizes process data from optimization iterations to learn the mapping relationship between different oil groove patterns and their load-carrying capacity. Then, the AI takes the currently found optimal oil groove pattern as a template (input), and adds disturbances provided by the swarm intelligence algorithm, thereby mutating multiple possibly better oil groove patterns. Subsequently, these oil groove patterns are provided for the GPS algorithm to evaluate and make decisions.

The optimal oil groove pattern is obtained using the above intelligent self-evolving design method, which approximates the shape of an arc-shaped side H instead of the traditional circular shape. The novel oil groove and traditional oil groove patterns from two major motor manufacturers are tested under different operating conditions using the quasi-actual friction pair test rig. The experiment results prove the high load-bearing advantage of the novel oil groove. In detail, the novel oil groove can reduce the maximum friction torque of the roller-piston pair by 88% (35 MPa, 30 rpm). At 35 MPa-0.5 rpm, the maximum friction torque reduction is 28%. This significant performance enhancement validates that the proposed self-evolving design method effectively overcomes the limitations of conventional design paradigms, which are constrained by initial shape assumptions and local optimization.

Acknowledgements

The authors acknowledge the financial support from the Key Program of the National Natural Science Foundation of China (No. 52435002), and the Second Batch Funding of Civil Aerospace Projects during the 14th Five-Year Plan Period (No. D020110).

Declaration of competing interest

The authors have no competing interests to declare that are relevant to the content of this article.

References

[1] Basavaraja J S, Sharma S C, Jain S C. A study of misaligned electrorheological fluid lubricated

hole-entry hybrid journal bearing. *Tribol Int* **43**(5): 1059-1064 (2010)

[2] Zhang C, Zhang X, Dong P, Zhang H, Zheng Z, Zhang J, Xu B. Composite thermal oil film lubrication model for hybrid journal bearings. *Tribol Int* **194**: 109556 (2024)

[3] Liang Y, Chen W, Sun Y, Yu N, Zhang P, Liu H. An expert system for hydro/aero-static spindle design used in ultra precision machine tool. *Robot Comput Integr Manuf* **30**(2): 107-113 (2014)

[4] Quaranta E, Davies P. Emerging and innovative materials for hydropower engineering applications: turbines, bearings, sealing, dams and waterways, and ocean power. *Engineering (Beijing)* **8**: 148-158 (2022)

[5] Nicodemus E R, Sharma S C. Orifice compensated multirecess hydrostatic/hybrid journal bearing system of various geometric shapes of recess operating with micropolar lubricant. *Tribol Int* **44**(3): 284-296 (2011)

[6] Huang X, Lin S, Liang J. Modelling approach of hybrid air herringbone grooved journal bearing considering the angular misalignment and centrifugal expansion. *Tribol Int* **189**: 108928 (2023)

[7] Meng F, Huang Q, Yu Z, Chen X, Fan X, Zhang W, Ming A. Explosive electric actuator and control for legged robots. *Engineering (Beijing)* **12**: 39-47 (2022)

[8] Vignesh G, Barik D, Sharma P, Medhi B J, Bora B J. Numerical investigation and optimization of the geometric profiles of dimple bottom structure in frictional interaction pairs. *Tribol Int* **185**: 108530 (2023)

[9] Zhang Y, Chen W, Yang X, Li Z, Dai B, Zhang J, Yang J, Li D. Effect of crescent-shaped texture based on different depths and orientations on the frictional properties of cam tappets. *Journal of Materials Research and Technology* **31**: 1826-1836 (2024)

[10] Shaohua L, Xiaohui L, Shuyun J. A lubrication model for bubbly oil lubrication with interfacial effect and thermal effect using the theory of multiphase mixtures. *Friction* **12**(2): 271-290 (2024)

[11] Khatri C B, Sharma S C. Analysis of textured multi-lobe non-recessed hybrid journal bearings with various restrictors. *Int J Mech Sci* **145**: 258-286 (2018)

[12] Liu Z, Wang Y, Cai L, Zhao Y, Cheng Q, Dong X. A review of hydrostatic bearing system: researches and applications. *Adv Mech Eng* **9**(10): 2071942141 (2017)

[13] Tomar A K, Sharma S C. An investigation into surface texture effect on hole-entry hybrid spherical journal bearing performance. *Tribol Int* **151**: 21 (2020)

[14] Sahu K, Sharma S C, Tomar A K. Analysis of MR fluid lubricated slot entry hybrid conical journal bearing with texturing arrangements. *Tribol Int* **188**: 17 (2023)

[15] Wang J, Huang J, Jiang S, Kouediatouka A N, Liu Q, Dong G. Analysis of maximum radial load capacity of hydrostatic journal bearing considering supply pressure limitation by a novel method. *Tribol Int* **184**: 108484 (2023)

[16] Yu Y, Pu G, Jiang T, Jiang K. A dragonfly wing inspired biomimetic aerodynamic thrust bearing for increased load capacity. *Int J Mech Sci* **176**: 105550 (2020)

[17] Sun W, Shi X, Lu X, Hua D, Li R, Liu H. Coupling analysis of timing gear dynamics and three-dimensional mixed lubrication under multi-branch shafting of marine diesel engine. *Structures* **58**: 105351 (2023)

[18] Feng K, Wang G, An C, Chen R, Li W, Huang S, Jiang J. Design and analysis of biomimetic micro-groove aerostatic bearing inspired by populus euphratica veins for enhanced load capacity and stiffness. *Precision Engineering* **93**: 18-36 (2025)

[19] Wang X, Shi L, Dai Q, Huang W, Wang X. Multi-objective optimization on dimple shapes for gas face seals. *Tribol Int* **123**: 216-223 (2018)

[20] Zhang J, Shen Y, Gan M, Su Q, Lyu F, Xu B, Chen Y. Multi-objective optimization of surface texture for the slipper/swash plate interface in eha pumps. *Front Mech Eng* **17**(4): 48 (2022)

[21] Guirguis D A M H K. Image matching assessment of attainable topology via kriging-interpolated level-sets. In: ASME 2014 International Design Engineering Technical Conferences and Computers and Information in Engineering Conference, 2014.

[22] Zhang C, Zhang X, Dong P, Zhang H, Zheng Z, Zhang J, Xu B. Composite thermal oil film

lubrication model for hybrid journal bearings. *Tribol Int* **194**: 109556 (2024)

[23] Audet C, Dennis J E. Mesh adaptive direct search algorithms for constrained optimization. *SIAM J Optim* **17**(1): 188-217 (2006)

[24] Bogani C, Gasparo M G, Papini A. Generalized pattern search methods for a class of nonsmooth optimization problems with structure. *J Comput Appl Math* **229**(1): 283-293 (2009)

[25] Lomonaco V, Maltoni D. Identification of abnormal tribological regimes using a microphone and semi-supervised machine-learning algorithm. *Friction* **10**(4): 583-596 (2022)

[26] Douimia S, Bekrar A, Ait El Cadi A, El Hillali Y, Fillon D. Machine learning and deep learning applications in the automotive manufacturing industry: a systematic literature review and industry insights. *Robot Comput Integr Manuf* **96**: 103034 (2025)

[27] Tang S, Zhu Y, Yuan S. Intelligent fault identification of hydraulic pump using deep adaptive normalized CNN and synchrosqueezed wavelet transform. *Reliab Eng Syst Saf* **224**: 108560 (2022)

[28] Ding X, Zhang X, Han J, Ding G. Scaling up your kernels to 31x31: revisiting large kernel design in CNNs. *2022 IEEE/CVF CONFERENCE ON COMPUTER VISION AND PATTERN RECOGNITION (CVPR)*: 11953-11965 (2022)

[29] Xu X, Zhang J, Huang W, Yu B, Lyu F, Zhang X, Xu B. The loose slipper fault diagnosis of variable-displacement pumps under time-varying operating conditions. *Reliab Eng Syst Saf* **252**: 110448 (2024)

[30] Lu X, Jiang Q, Shen Y, Lin X, Xu F, Zhu Q. Enhanced residual convolutional domain adaptation network with CBAM for rul prediction of cross-machine rolling bearing. *Reliab Eng Syst Saf* **245**: 109976 (2024)

[31] Ding X, Zhang Y, Ge Y, Zhao S, Song L, Yue X, Shan Y. Unireplknet: a universal perception large-kernel convnet for audio, video, point cloud, time-series and image recognition. *2024 IEEE/CVF CONFERENCE ON COMPUTER VISION AND PATTERN RECOGNITION, CVPR 2024*: 5513-5524 (2024)

[32] Suganthan P N. Particle swarm optimiser with neighbourhood operator. In: 1999: 1958-1962.

[33] Wang D, Tan D, Liu L. Particle swarm optimization algorithm: an overview. *Soft comput* **22**(2): 387-408 (2018)

[34] Zhang X, Zhang J, Zeng D, Zhao J, Xu B, Zhang C. A quasi-actual mechatronic instrument for realistically testing roller-piston friction pairs. *IEEE/ASME Transactions on Mechatronics* **29**(2): 1240-1248 (2024)

Xiaolong Zhang: Received the Ph.D. degree in mechanical engineering from Zhejiang University, Hangzhou, China, in 2025. He currently serves as an Assistant Researcher at Zhejiang University in Hangzhou, China. His research interests include the design of high-efficiency hydraulic motors and intelligent high-load-bearing structures.

Kaiming Zheng: Received the B.S. degree in mechanical engineering from Central South University in 2025. Currently pursuing a Ph.D. in Mechanical Engineering at Zhejiang University in Hangzhou, China. His research interests include modeling and optimization design of high-load friction pairs in hydraulic motors.

Hongbin Lin: Received the B.S. degree in mechanical engineering from Dalian University of Technology in 2023. Currently pursuing a Ph.D. in Mechanical Engineering at Zhejiang University in Hangzhou, China. His research interests focus on enhancing the durability of guide rails in internal-curve hydraulic motors.

Junhui Zhang: Received the B.S. and Ph.D. degrees in mechanical engineering from Zhejiang University, Hangzhou, China, in 2007 and 2012, respectively. He is currently a professor with the Institute of Mechatronics and Control Engineering and the Deputy Director of the State Key Laboratory of Fluid Power Transmission and Control, Zhejiang University. He published more than 40 papers indexed by SCI, and applied for more than 20 National Invention Patents with 18 granted. He is supported by the National Science Fund for Distinguished Young Scholars. His research interests include high-speed hydraulic pumps/motors and hydraulic robots.

Bing Xu: Received the Ph.D. degree in fluid power transmission and control from Zhejiang University, Hangzhou, China, in 2001. He is currently a Professor and a Doctoral Tutor with the Institute of Mechatronic Control Engineering, and the Director of the State Key Laboratory of Fluid

Power Transmission and Control, Zhejiang University. He has authored or coauthored more than 200 journal and conference papers and has been awarded 49 patents. He is a Chair Professor of the Yangtze River Scholars Programme and a science and technology innovation leader of the Ten Thousand Talent Programme.

Huayong Yang: Academician of the Chinese Academy of Engineering and expert in fluid transmission and control. Currently serves as Director of the School of Engineering at Zhejiang University, Director of the State Key Laboratory of Fluid Power Components and Mechatronic Systems, President of the International Alliance for Intelligent Manufacturing, and Vice President of the Chinese Mechanical Engineering Society. He has conducted extensive research in fundamental theories of electro-hydraulic control, efficient design of core components and systems, as well as the development and engineering application of key technologies for shield tunneling equipment. His work has established a comprehensive technological pathway encompassing "theory-components-systems-equipment-application".

Chao Zhang*: Received the B.S. and M.S. degrees in material science and engineering from Northwestern Polytechnical University, Xi'an, China, in 2017 and 2020, respectively, and the Ph.D. degree in mechanical engineering from the University of Lyon, Lyon, France, in 2012.He is currently a research fellow with the Institute of Mechatronics and Control Engineering, Zhejiang University. He published more than 60 papers indexed by SCI. He is supported by the National Science Fund for

Excellent Young Scholars. His research interests include high-performance electro-hydraulic actuators and robotics.